





## Article

# Tubular C<sub>3</sub>N<sub>4</sub> Nanotubes as Metal-Free Sulfur Hosts toward Stable Lithium–Sulfur Batteries

Chaoqi Zhang <sup>1</sup>, Ruifeng Du <sup>1,2</sup>, Sara Martí-Sánchez <sup>3</sup>, Ke Xiao <sup>1,2</sup>, Dawei Yang <sup>1,2,4</sup>, Chaoyue Zhang <sup>1</sup>, Canhuang Li <sup>1,5</sup>, Guifang Zeng <sup>1,2</sup>, Xingqi Chang <sup>1,5</sup>, Ren He <sup>1,2</sup>, Jordi Arbiol <sup>3</sup>, Junshan Li <sup>6</sup>, Jordi Jacas Biendicho <sup>1,\*</sup> and Andreu Cabot <sup>1,7,\*</sup>

- <sup>1</sup> Catalonia Institute for Energy Research–IREC, Sant Adrià de Besòs, 08930 Barcelona, Spain; czhang@irec.cat (C.Z.); kexiao@irec.cat (K.X.); czhang@irec-edu.cat (C.Z.); canhuangli2020@gmail.com (C.L.); zengguifangjennifer@gmail.com (G.Z.); xchan@irec.cat (X.C.); grenhe@irec-edu.cat (R.H.)
- <sup>2</sup> Department of Physics, Universitat de Barcelona, 08028 Barcelona, Spain
- <sup>3</sup> Catalan Institute of Nanoscience and Nanotechnology (ICN2), CSIC and BIST, Campus UAB, Bellaterra, 08193 Barcelona, Spain; sara.marti@icn2.cat (S.M.-S.); arbiol@icrea.cat (J.A.)
- <sup>4</sup> Henan Key Laboratory of Photovoltaic Materials, Henan University, Kaifeng 475004, China
- <sup>5</sup> Department of Chemistry, Universitat de Barcelona, 08028 Barcelona, Spain
- <sup>6</sup> Institute of Advanced Study, Chengdu University, Chengdu 610106, China; lijunshan@foxmail.com
- <sup>7</sup> ICREA, Pg. Lluís Companys 23, 08010 Barcelona, Spain
- \* Correspondence: jjacas@irec.cat (J.J.B.); acabot@irec.cat (A.C.)

**Abstract:** Lithium–sulfur batteries (LSBs) with high energy density have the potential to replace current commercial lithium-ion batteries. However, the shuttle effect and the low conversion kinetics of lithium polysulfide (LiPS) remain the main challenges in the development of LSBs. In this study, a metal-free and simple-to-prepare carbon nitride with a high surface area and tubular morphology (CN-nt) is used as the sulfur host for LSBs. Due to its unique nanostructure and rich active sites, it not only effectively disperses the active sulfur material and anchors soluble polysulfide species, but it also promotes the nucleation process of Li<sub>2</sub>S, thus achieving fast and sustainable Li-S redox reactions. Experimental results show that the obtained S@CN-nt electrodes exhibit a high sulfur utilization of 1296.2 mAh g<sup>-1</sup> at 0.1 C and a significant rate capability of 689.4 mAh g<sup>-1</sup> at the high current rate of 3C. More importantly, the capacity retention reaches 87.7% after 500 cycles. This simple strategy of engineering unique carbon-based nanostructured hosts can inspire new ideas for developing cost-effective and metal-free host materials for sulfur-based batteries.

**Keywords:** carbon nitride; nanotube; nanosheet; lithium–sulfur battery; energy storage material



**Citation:** Zhang, C.; Du, R.; Martí-Sánchez, S.; Xiao, K.; Yang, D.; Zhang, C.; Li, C.; Zeng, G.; Chang, X.; He, R.; et al. Tubular C<sub>3</sub>N<sub>4</sub> Nanotubes as Metal-Free Sulfur Hosts toward Stable Lithium–Sulfur Batteries. *Energies* **2023**, *16*, 4545. <https://doi.org/10.3390/en16124545>

Academic Editor: Massimo Guarnieri

Received: 26 April 2023

Revised: 27 May 2023

Accepted: 30 May 2023

Published: 6 June 2023



**Copyright:** © 2023 by the authors. Licensee MDPI, Basel, Switzerland. This article is an open access article distributed under the terms and conditions of the Creative Commons Attribution (CC BY) license (<https://creativecommons.org/licenses/by/4.0/>).

## 1. Introduction

The existence of portable power sources mainly associated with the development of lithium-ion batteries (LIBs) has brought great convenience to our daily life [1,2]. However, after over 30 years of development, LIBs are experiencing a bottleneck in energy density improvement (theoretical value 420 Wh kg<sup>-1</sup>, based on graphite anodes and LiNi<sub>1/3</sub>Mn<sub>1/3</sub>Co<sub>1/3</sub>O<sub>2</sub> cathodes) [3], and the rising raw material prices are increasing the cost pressure [4]. Lithium–sulfur batteries (LSBs), with high potential energy density (2500 Wh kg<sup>-1</sup>) and low-cost materials, can meet the rapidly growing demand in the fields of electric vehicles and smart grids [5]. However, the practical application of Li-S batteries is limited by several inherent challenges in the sulfur cathode [6]. Firstly, lithium polysulfides (LiPSs) as intermediate products in the Li-S reaction process dissolve in the electrolyte and cause a shuttle effect, resulting in irreversible sulfur loss and negative electrode corrosion [7]. Secondly, in the lithiation process, up to 80% volume expansion of Li<sub>2</sub>S compromises the structural stability, leading to electrode structure collapse and eventual failure [8]. Thirdly, S/Li<sub>2</sub>S with electronic/ion insulation characteristics cannot achieve

sufficient dispersion to obtain good utilization [9]. At the same time, the slow reaction kinetics in the Li-S multi-electron reaction process also needs to be improved urgently [10].

To overcome the above challenges, a series of strategies have been developed over the past decade, among which the use of sulfur hosts is the most extensively studied strategy [11]. Carbon materials, including mesoporous carbon, graphene, and carbon nanotubes, as the earliest studied hosts, could uniformly disperse sulfur-active materials through their high specific surface area and high electrical conductivity, ultimately improving sulfur utilization and mitigating volume expansion [12]. However, the weak physical interaction between polar LiPSs and non-polar carbon materials cannot suppress the severe shuttle effect of LiPSs. Although a series of transition metal compound materials has been investigated in the past several years to utilize their polar surfaces to suppress shuttle effects, some drawbacks still cannot be avoided, such as lower specific surface area products and a complex preparation process, accompanied by the generation of toxic pollutants. Therefore, employing metal-free host materials through a simple preparation procedure has become a direction worthy of exploration to address the current challenges in LSBs. Efficient chemical adsorption of LiPSs can be achieved by heteroatom doping of carbon materials, which has been extensively studied in recent years [13]. Taking nitrogen as an example, the doped nitrogen atoms work as effective active sites to chemically adsorb Li atoms of LiPS through Lewis acid–base coupling, thereby inhibiting the shuttle effect of LiPS. However, even with various complex procedures, the nitrogen content in current nitrogen-doped carbon materials is still very low (less than 10 wt%). Therefore, further development is needed to achieve high-nitrogen-content carbon-based hosts through a simple method.

Similar to graphene, graphitic carbon nitride ( $g\text{-C}_3\text{N}_4$ ) is another representative two-dimensional (2D) layered material [14]. It has attracted widespread attention due to its excellent chemical stability, ease of synthesis, and low cost. Theoretically,  $g\text{-C}_3\text{N}_4$  has a high nitrogen content of up to 60 wt%, including  $\text{N}(\text{C})_3$  and  $\text{C}=\text{N}-\text{C}$  (pyridinic-N) species [15]. Density functional theory (DFT) calculations have shown that pyridinic-N has a much stronger chemical interaction with LiPS compared to other forms of nitrogen [16,17]. However, it is worth noting that although  $g\text{-C}_3\text{N}_4$  theoretically possesses an ultra-high specific surface area similar to graphene, conventional synthesis methods cannot exploit this advantage. For example, with the most traditional calcination and liquid exfoliation method, the obtained carbon nitride nanosheets (CN-ns) suffer from severe Van der Waals forces-induced restacking, resulting in unsatisfactory specific surface area (even lower than  $30\text{ m}^2\text{ g}^{-1}$ ) [18]. By designing alternative nanostructures with more rigid architectures, such as nanotubes, the intrinsic structural rigidity can avoid the aggregation of layered materials, while the associated increase in pore volume can contribute to effective buffering of the electrode material volume expansion [19]. Additionally, an interconnected structure is also advantageous for the rapid diffusion of  $\text{Li}^+$ . Currently, the template method is an effective means of obtaining unique nanostructured  $g\text{-C}_3\text{N}_4$  [16]. However, the additional cost of the template material and subsequent removal steps undoubtedly increase the cost pressure, especially in a material-intensive industry such as batteries.

In this paper, a simple one-step method is detailed for the preparation of carbon nitride nanotubes (CN-nt) with high specific surface area and porosity, which are applied as a metal-free sulfur-host material in LSBs. Unlike the conventionally prepared carbon nitride nanosheets (CN-ns), the CN-nt, characterized by higher surface areas and a tubular structure, improve the distribution of sulfur, effectively increasing the utilization of active materials. At the same time, the extensively exposed pyridinic-N active sites provide strong trapping of LiPS and accelerate the conversion process. Therefore, S@CN-nt cathodes exhibit excellent rate performance and cycling stability, demonstrating unique advantages in the application of Li-S batteries from the perspective of nanostructures.

## 2. Materials and Methods

Preparing CN-nt and CN-ns. The synthesis of CN-nt was achieved via a one-step calcination method. In this process, 10 g of urea (99.5%, ACROS Organics, Geel, Belgium)

and 1 g of melamine (99%, ACROS Organics) were thoroughly ground for 15 min using a mortar to create a white precursor mixture. The resulting mixture was then placed in a crucible covered loosely with a lid and annealed at 550 °C for 4 h in a muffle furnace under a standing air atmosphere, with a heating rate of 5 °C min<sup>-1</sup>. Following natural cooling to room temperature, the resulting 0.72 g light-yellow powder was collected without further treatment (ca. 6.5% yield). CN-ns were also synthesized via the same annealing method, only using melamine as the precursor. Subsequently, the obtained yellow powder was ground into fine particles and subjected to 2 h of ultrasonic treatment to produce the CN-ns (ca. 16.2% yield).

Synthesis of S@CN-nt, S@CN-ns. Typically, CN-nt and CN-ns are mixed with sulfur powder (Sigma Aldrich, Burlington, MA, USA, 99.98%) separately by the weight ratio of 1:3, and then the mixture is heated at 155 °C overnight in an autoclave under Ar protection.

### 3. Results and Discussion

A precursor regulation strategy is used for the preparation of different carbon nitrides. As shown in Figure 1a,b, scanning electron microscope (SEM) images indicate that CN-ns and CN-nt samples have different morphologies. The CN-ns sample is obtained by calcination of melamine precursor, followed by subsequent ultrasonic exfoliation, resulting in a stacked nanosheet morphology. In contrast, the CN-nt sample made by the precursor of urea and melamine mixture and subject to the same calcination step, without any subsequent treatment, resulted in a product with a hollow tube-shape morphology with a diameter of about 200–300 nm and a length of several micrometers. The formation mechanism of hollow g-C<sub>3</sub>N<sub>4</sub> nanotubes has been investigated before. In the pyrolysis process, urea is first converted to cyanuric acid at an initial rapid heating process. Then, through hydrogen bonding with melamine, supramolecular rod-shaped melamine–cyanuric acid is formed [20,21]. During the subsequent annealing process, the resulting collapse occurs from the center of the nanorod along the tube wall direction, thus forming hollow tubular CN-nt [22]. Energy dispersive spectrometry (EDS) compositional maps indicate that the C and N elements are evenly distributed both in CN-nt (Figure 1e) and CN-ns (Figure S1) samples. Transmission electron microscopy (TEM) images provide more detailed morphological information, as shown in Figure 1c, where the CN-nt exhibit a wrinkled outer wall. The internal hollow structure can be recognized by the cross-sectional TEM image in Figure 1c, which allows for calculating a tube wall thickness of about 30–40 nm. Furthermore, electron energy loss spectroscopy (EELS) analysis confirmed the homogeneous distribution of C and N (Figure 1f).

X-ray diffraction (XRD) analysis shows that CN-ns and CN-nt samples exhibit identical diffraction peaks at 12.9° and 27.75° corresponding to the characteristic diffraction planes of the (100) and (002) of g-C<sub>3</sub>N<sub>4</sub> (Figure 1d) [23]. The nitrogen adsorption–desorption isotherms of CN-ns and CN-nt are displayed in Figure 1g. According to the Barrett–Joyner–Halenda model, CN-nt have a high specific surface area of 198.78 m<sup>2</sup> g<sup>-1</sup>, well above that of CN-ns at 33.27 m<sup>2</sup> g<sup>-1</sup>. Similarly, a significant difference in pore volume between the two samples can be found, with the CN-nt sample displaying a much larger pore volume of 0.89 cm<sup>3</sup> g<sup>-1</sup> than CN-ns (0.17 cm<sup>3</sup> g<sup>-1</sup>). These results demonstrate that the unique hollow tubular structure of CN-nt helps to overcome the stacking limitation of CN-ns driven by Van der Waals forces. Table S1 shows the differences in the synthetic method, specific surface area, and pore volume of g-C<sub>3</sub>N<sub>4</sub> obtained by different methods. It is clear from the list that this one-step pyrolysis of urea and melamine mixture has unique advantages. The thermal stability of the CN-nt was also verified by conducting and analyzing thermogravimetric analysis (TGA) and derivative thermogravimetry (DTG) results, as illustrated in Figure 1h. The calcination process under N<sub>2</sub> atmosphere showed that CN-nt were thermally stable at temperatures below 550 °C. At this temperature, the weight started to slowly decrease, but the fastest weight loss occurred at around 725 °C. CN-nt were completely decomposed at around 770 °C. This result is consistent with previous reports about g-C<sub>3</sub>N<sub>4</sub> [24], proving that the hollow tubular structure does not decrease the thermal stability of g-C<sub>3</sub>N<sub>4</sub>.

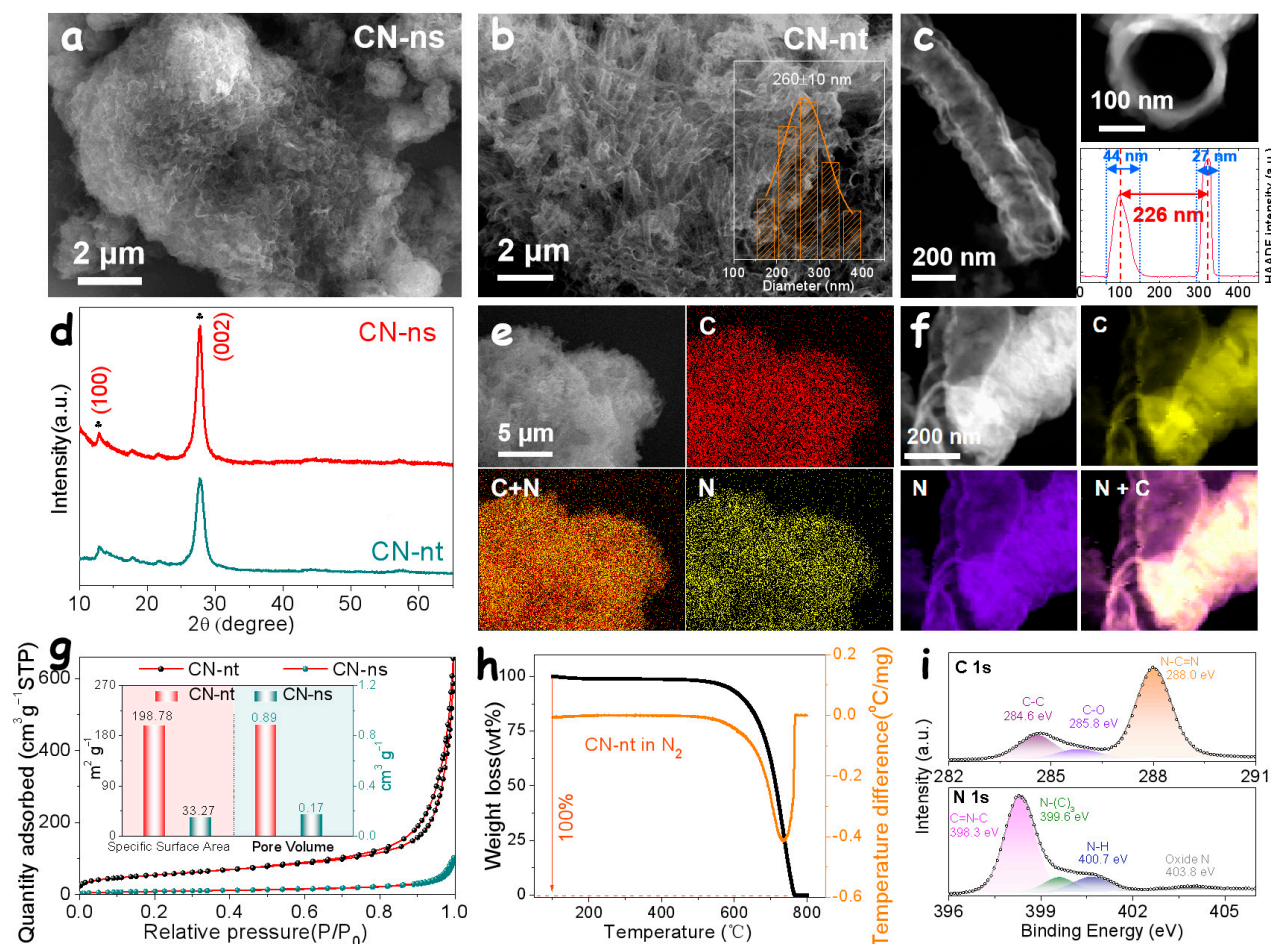


**Figure 1.** (a) SEM image of CN-ns. (b) SEM image of CN-nt. Inset histograms show the nanotube diameter distributions. (c) HADDF-STEM image of CN-nt. (d) XRD pattern of CN-ns and CN-nt. (e) SEM image and EDS mapping image of CN-nt. (f) HADDF-STEM image and EELS compositional mapping of CN-nt. (g)  $N_2$  adsorption–desorption isotherms of CN-nt and CN-ns. Inset shows the specific surface area and pore volume of CN-nt and CN-ns. (h) TGA and DTG curves. (i) XPS spectra of C1s and N1s.

XPS analyses were used to determine the surface composition and chemical states. Figure S2 shows that both CN-ns and CN-nt samples are mainly composed of C and N, with a small amount of O associated with the inevitable exposure to air. The proportion of nitrogen elements in CN-nt and CN-ns is close, at 50.5% and 56.3%, respectively. Figure 1i exhibits the C1s and N1s spectra of CN-nt, and the C1s spectrum can be fitted with three peaks at binding energies of 284.6, 285.8, and 288.0 eV, which are attributed to pure graphitic sites in the carbon nitride matrix (C–C), the  $sp_2$ -hybridized carbon atoms bonded to N in an aromatic ring (C–N–C), and the  $sp_2$ -hybridized carbon in the aromatic ring attached to the  $NH_2$  group (N–C=N) [25]. The N1s spectrum can be deconvoluted into four peaks, ascribable to pyridinic-N (C=N–C) at 398.3 eV, N–(C)<sub>3</sub> at 399.6 eV, N–H at 400.7 eV, and oxygen-N at 403.8 eV [26]. Overall, XPS analyses show that CN-nt contain a large number of pyridinic-N species, which are expected to have a favorable effect on the confinement of the LiPS shuttle effect and thus favor stable LSB performance.

To prepare the cathode material, sulfur was introduced into the CN-nt via a melt diffusion method. The XRD diffraction pattern in Figure S3 demonstrates the presence of abundant sulfur crystals in S@CN-nt, while the TGA curve shows a 73.7% mass loss in S@CN-nt before 350 °C, corresponding to the mass fraction of S in the composite. SEM images and the corresponding EDX elemental maps revealed that the tubular structure of



CN-nt was preserved in S@CN-nt, and the S element exhibited a homogeneous distribution without independent S particles or major aggregates. This result demonstrates that CN-nt, with their high surface area and hollow tubular structure, serve as a sulfur host to achieve a uniform distribution. The same experimental data obtained for S@CN-ns (Figure S4) showed a less uniform dispersion of S in this sample.

Visualizing the adsorption behavior of soluble LiPS is beneficial for understanding the adsorption capacity of the host material and validating its shuttle effect inhibition. Equal amounts of Super P, CN-ns, and CN-nt were immersed in the same amount of a 5 mM  $\text{Li}_2\text{S}_4$  solution and left undisturbed overnight. After this time, compared to the brownish-red  $\text{Li}_2\text{S}_4$  solution, CN-nt showed a clear supernatant, indicating that soluble  $\text{Li}_2\text{S}_4$  species were adsorbed by the CN-nt material (Figure 2a). This high adsorption is related to the high specific surface area and its polar nature associated with the presence of nitrogen. In particular, the presence of Lewis-base pyridine nitrogen in g- $\text{C}_3\text{N}_4$  helps to interact with the strong Lewis-acid of terminal Li atoms in LiPS [27]. In contrast, a slightly yellowish supernatant was observed in the CN-ns vial, demonstrating that the CN-nt with a higher specific surface area have a stronger adsorption capacity. The supernatant color of Super P is similar to that of LiPS, indicating that Super P composed of non-polar graphite surfaces cannot work for LiPS capture [28]. As shown in the UV-vis absorption spectra of the supernatant (Figure 2b), the 400–450  $\text{cm}^{-1}$  band region is the fingerprint of the  $\text{Li}_2\text{S}_4$  absorption spectra [29], in which CN-nt exhibited the lowest intensity, indicating the lowest content of  $\text{Li}_2\text{S}_4$  in the supernatant and proving the best adsorption capacity. Furthermore, the XPS N1s spectra of the CN-nt sample were also compared and analyzed, both before and after adsorption of  $\text{Li}_2\text{S}_4$  (Figure 2c), and it was found that the peak assigned to pyridinic nitrogen shifted from 398.3 eV to 398.45 eV, which is attributed to the fact that LiPS can anchor on active nitrogen sites through dipole–dipole interactions, consistent with previous reports [27].

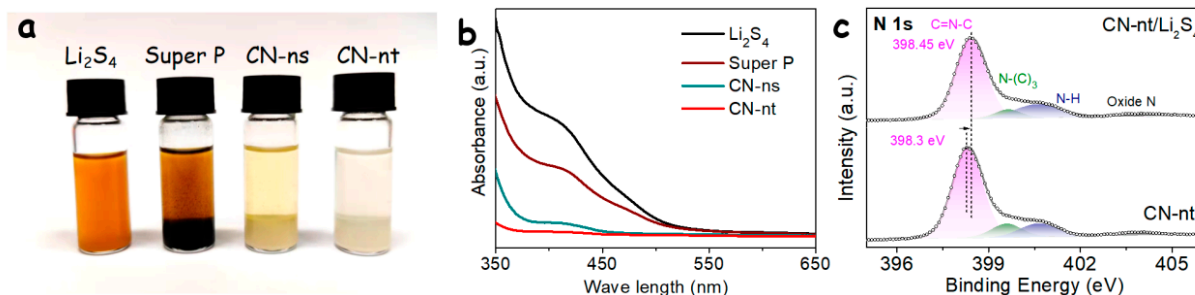


**Figure 2.** (a) Photograph and (b) UV-vis spectra of the polysulfide solution after exposure to the different adsorbers. (c) High-resolution XPS N1s spectra before and after adsorption of  $\text{Li}_2\text{S}_4$ .

Considering the complexity of the multi-electron transfer process in the Li-S reaction, evaluating the electrocatalytic activity of host materials during the redox process can effectively forecast the performance of LSBs [30,31]. In this direction, symmetric cell tests based on different host materials were assembled and tested. As shown in Figures 3a and S5, in the symmetric cell test without polysulfide, CN-nt show a very low response current and the rectangular CV curve confirms that only double-layer adsorption occurs on their surface [32]. When adding  $\text{Li}_2\text{S}_6$  into the electrolyte, both CN-ns and CN-nt exhibit polysulfide oxidation-reduction signals in the CV curve. However, CN-nt show significantly higher oxidation-reduction current and more pronounced oxidation-reduction peaks, indicating that CN-nt have higher activity in promoting the Li-S reaction compared to CN-ns.

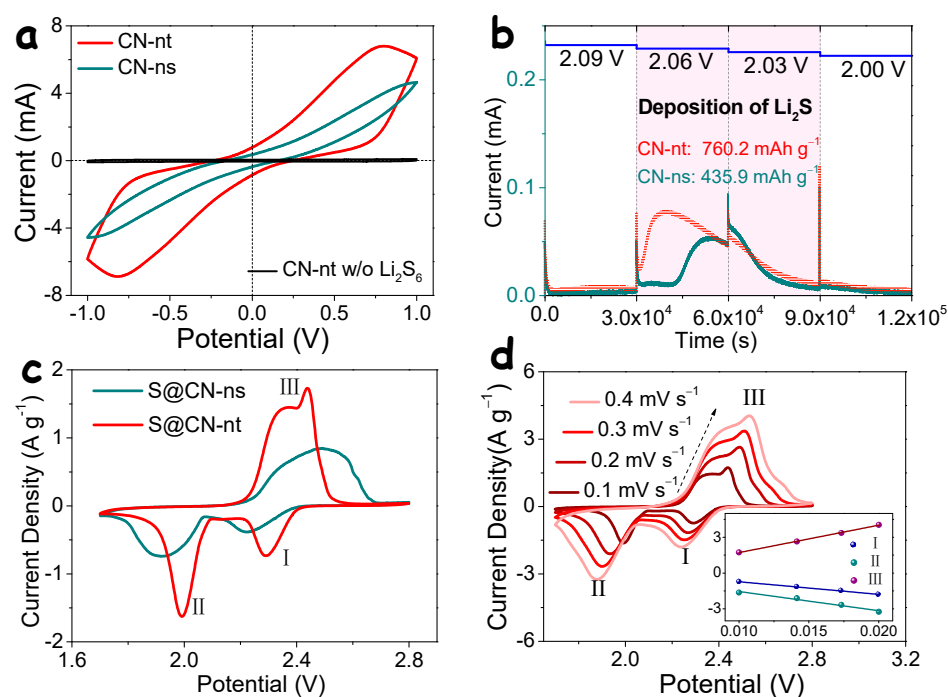


**Figure 3.** (a) CV profiles of symmetrical cells with different host materials using an electrolyte containing  $0.5 \text{ mol L}^{-1} \text{ Li}_2\text{S}_6$ . (b) PITT measurements of  $\text{Li} | \text{Li}_2\text{S}_8$  cells with different host materials, the cells were discharged from 2.09 to 2.00 V with a step of 30 mV. (c) CV curves of different cathodes in a coin cell. (d) CV curves of  $\text{S@CN-nt}$  cathode under various scan rates. The inset plot is the CV peak current density (Y axial,  $\text{A g}^{-1}$ ) for peaks I, II, and III; versus the square root of the scan rates (X axial,  $(\text{V s}^{-1})^{0.5}$ ).

In the discharge process of an LSB, the theoretical contribution of the transition from liquid  $\text{Li}_2\text{S}_4$  to solid  $\text{Li}_2\text{S}$  can account for 75% of the capacity. Therefore, the potentiostatic intermittent titration technique (PITT) was used to quantitatively study the promoting effect of host materials in the deposition process [33,34]. During the PITT test, the cathode with an electrolyte containing 0.25 M  $\text{Li}_2\text{S}_8$  was subjected to pulse discharge at different voltages, and the corresponding response current is shown in Figure 3b. Due to the fast redox kinetics of  $\text{LiPS}$  in the solution state, a sharp current response was observed in both CN-ns and CN-nt cells during the 2.09 V potentiostatic process, followed by a rapid decline and gradual stabilization. In the subsequent 2.06 V potentiostatic process related to the electrochemical phase transition reaction, both cells showed a response current peak except for the initial rapid response and decay, indicating that the solid products of  $\text{Li}_2\text{S}/\text{Li}_2\text{S}_2$  were precipitated from the electrolyte containing  $\text{LiPS}$  with the prolongation of the constant voltage time at 2.06 V.

The nucleation and growth of  $\text{Li}_2\text{S}/\text{Li}_2\text{S}_2$  crystals are closely related to the inherent nucleation sites on the substrate [35,36]. Due to their higher specific surface area and unique tubular structure, CN-nt provide abundant nucleation sites, which effectively accelerates the nucleation kinetics of  $\text{Li}_2\text{S}/\text{Li}_2\text{S}_2$ . Consequently, compared with CN-ns, the CN-nt host exhibits a higher current response (approximately 50% increase in current density) at 2.06 V, as well as an earlier peak response time (approximately ahead 14,700 s). The insulating nature of  $\text{Li}_2\text{S}/\text{Li}_2\text{S}_2$  hinders the capacity to release during the discharge process. Therefore, based on Faraday's law, the current vs. time curves were integrated for the phase transition discharge process from 2.09 to 2.00 V to quantitatively analyze the liquid–solid phase transformation capacity. The results show that the CN-nt-related cell can release a capacity of  $760.2 \text{ mAh g}^{-1}$ , while only  $435.9 \text{ mAh g}^{-1}$  in the CN-ns cell. These results demonstrate the promoting effect of CN-nt on the  $\text{Li}_2\text{S}$  nucleation process, which is beneficial for the performance of LSBs.

Subsequently, coin-type LSBs were assembled using S@CN-ns and S@CN-nt cathodes. As shown in the cyclic voltammetry (CV) curves (Figure 3c), both S@CN-ns and S@CN-nt electrodes exhibit two reduction peaks, which correspond to the transformation of S<sub>8</sub> into long-chain Li<sub>2</sub>S<sub>x</sub> ( $4 \leq x \leq 8$ ) and subsequent conversion to insoluble Li<sub>2</sub>S<sub>2</sub>/Li<sub>2</sub>S. The anodic peak during the oxidation process corresponded to the conversion of solid Li<sub>2</sub>S/Li<sub>2</sub>S<sub>2</sub> to long-chain soluble LiPS and finally to S<sub>8</sub>. By comparing the CV curves, it was evident that the S@CN-nt electrode exhibited a higher peak voltage than the S@CN-ns electrode during the reduction process. Peak I and II located at 2.290 and 1.992 V, respectively, were significantly higher than the 2.22 V and 1.919 V of S@CN-ns. In addition, compared to the 2.489 V of the S@CN-ns electrode, a significantly lower anodic peak voltage was shown at 2.438 V from the S@CN-nt electrode. Furthermore, the S@CN-nt electrode exhibited excellent current response, with a peak current density much higher than those of S@CN-ns at all three peaks. These results demonstrate that CN-nt, which have a higher specific surface area and porous structure, are more suitable as a sulfur host material than CN-ns and are therefore beneficial for improving the performance of LSBs.

As the scan rate of the CV curve increases, a shift of the redox peaks and the response of the current density is generally observed. In Figure 3d, with the scan rate increasing from 0.1 to 0.4 mV s<sup>-1</sup>, the reduction peak slightly shifts towards lower potential while the oxidation peak shifts towards higher potential, accompanied by an increasing current density. By fitting the current and square root of the scan rate, it can be found that the results show a good linear relationship, which is consistent with a diffusion limitation during the electrochemical test process [37,38]. Herein, the classical Randles–Sevchik equation for a semi-infinite diffusion can be applied [39,40], as shown below:

$$I_p = (2.69 \times 10^5) n^{1.5} A D_{Li^+}^{0.5} C_{Li^+} \nu^{0.5}$$

where  $I_p$  is the peak current (A),  $n$  is the charge-transfer number,  $S$  is the geometric area of the electrode (cm<sup>2</sup>),  $D_{Li^+}$  is the chemical diffusion coefficient (cm<sup>2</sup> s<sup>-1</sup>),  $C_{Li^+}$  is the concentration of electrolyte (mol cm<sup>-3</sup>), and  $\nu$  is the potential scan rate (V s<sup>-1</sup>). Based on this equation and the slope values from the inset plot of Figure 3d, the apparent diffusion coefficients for the peaks of I, II, and III are  $1.55 \times 10^{-7}$ ,  $3.52 \times 10^{-7}$ , and  $6.68 \times 10^{-7}$  cm<sup>2</sup> s<sup>-1</sup> [41].

Subsequently, the assembled coin cells were subjected to electrochemical impedance spectroscopy (EIS) testing. The Nyquist plot from fresh cells consists of a semicircle in the high-frequency region and an oblique line in the low-frequency region, corresponding to the charge transfer resistance and the Li<sup>+</sup> diffusion of the electrodes, respectively. It is clear that compared to the S@CN-ns electrode, the S@CN-nt electrode exhibits a smaller semicircle and a more sloping straight line, indicating a smaller charge transfer resistance and a faster Li<sup>+</sup> diffusion process in the S@CN-nt electrode [42]. The smaller charge transfer resistance is due to the efficient dispersion of insulating sulfur by the high surface area of the CN-nt structure, while the fast Li<sup>+</sup> diffusion process might be attributed to the fast Li<sup>+</sup> transport in the tubular and interconnected structure [37,43]. Therefore, the EIS results suggest that the CN-nt host with unique architecture has a promoting effect on the performance of LSBs.

The LSB performance was evaluated in a galvanostatic charge–discharge test at 0.1C. As shown in Figure 4a, both the S@CN-ns and S@CN-nt electrodes presented two discharge plateaus and one long charge plateau in the charge–discharge curves, corresponding to the two reduction peaks and one oxidation peak in the CV curves, respectively. Obviously, the S@CN-nt electrode exhibited a superior charge–discharge capacity, up to 1246 mAh g<sup>-1</sup>, which was significantly higher than the 1040 mAh g<sup>-1</sup> of the S@CN-ns electrode, proving the rationality of CN-nt material as a sulfur host. In addition, polarization voltage can be defined by the voltage difference at 50% discharge capacity to quantitatively evaluate the polarization situation of the cathode in the Li-S reaction [44,45]. The polarization voltage of the S@CN-nt electrode was 152 mV, much lower than the 223 mV of the S@CN-ns electrode, which could be explained by the uniform distribution of sulfur active materials

achieved by CN-nt and the abundant active sites provided for the  $\text{Li}_2\text{S}$  conversion process, thus effectively reducing the voltage polarization during the charge–discharge process. Moreover, during the discharge process, according to the electronic transfer theory, the second plateau represented the  $\text{Li}_2\text{S}_4 \rightarrow \text{Li}_2\text{S}$  conversion process and released 75% of the capacity. Therefore, considering the inadequacy of the  $\text{Li}_2\text{S}$  nucleation process, the ratio of the second plateau capacity Q2 to the first plateau capacity Q1 can quantitatively describe the conversion ability of LiPS to  $\text{Li}_2\text{S}$  [46,47]. According to the calculation, the value of Q2/Q1 corresponded to 2.31 in the S@CN-nt electrode, which was much higher than the 2.02 of the S@CN-ns electrode, thus verifying the promoting effect of the CN-nt host in the  $\text{Li}_2\text{S}$  nucleation process.

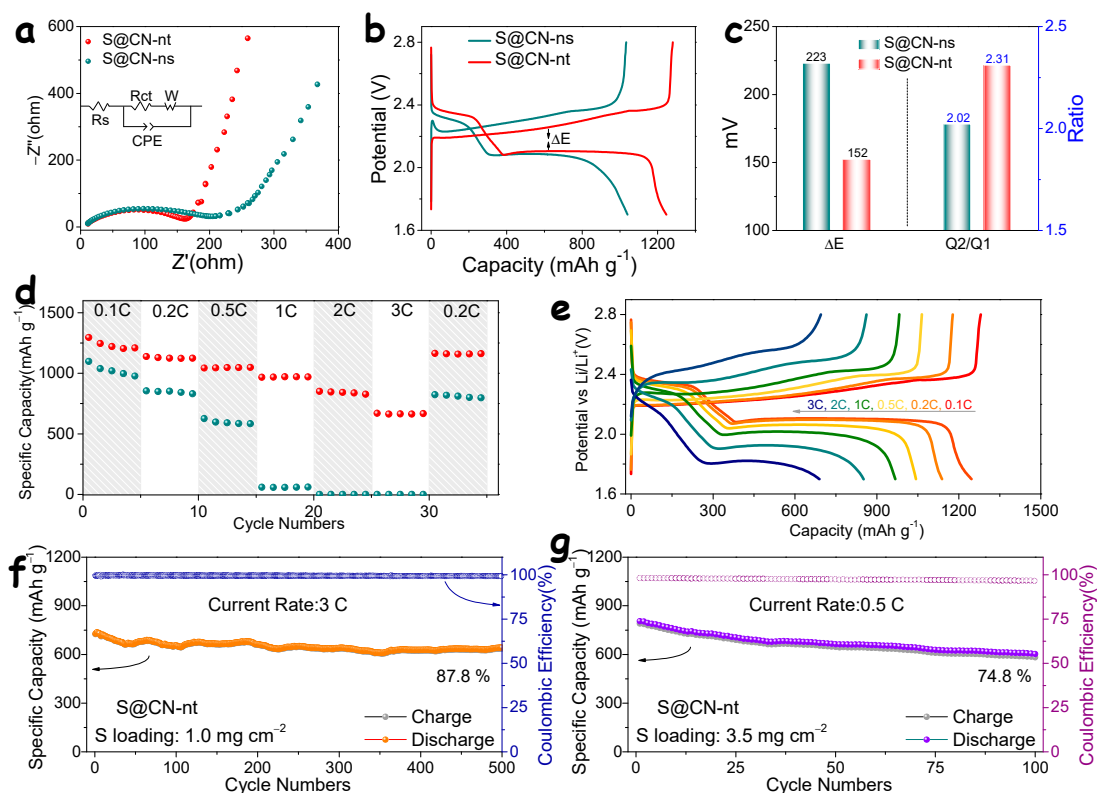


**Figure 4.** (a) EIS spectra of S@CN-ns and S@CN-nt electrodes. The Nyquist curves were fitted considering the equivalent circuits shown as inset, where  $R_s$ ,  $R_{ct}$ , and  $W$  stand for the resistance of the electrolyte, interfacial charge transportation, and semi-infinite Warburg diffusion, respectively; and CPE stands for the corresponding capacitance. (b) Charge/discharge curves of different electrodes at a current rate of 0.1 C in second cycles. (c) The value of  $\Delta E$  and Q2/Q1 obtained from charge/discharge curves. (d) Rate capability of the S@CN-ns and S@CN-nt cathodes at various current rates from 0.1 C to 3 C. (e) Charge/discharge curves of S@CN-nt at different current rates. (f) Capacity retention of S@CN-nt at 3 C for 500 cycles. (g) Cycling performance of electrodes with a  $3.5 \text{ mg cm}^{-2}$  sulfur loading.

Figure 4d displays the rate performance of the different electrodes. S@CN-nt achieved an initial capacity of  $1296.2 \text{ mAh g}^{-1}$  at a current density of 0.1C, much higher than the  $1098.9 \text{ mAh g}^{-1}$  of the S@CN-ns electrode. In addition, even at a higher current density of 3C, S@CN-nt still maintained a high discharge capacity, reaching up to  $689.4 \text{ mAh g}^{-1}$ , while the S@CN-ns electrode could not release any capacity. The polarization situation at different current densities can be understood by analyzing the charge–discharge curves. The S@CN-nt electrode exhibited two plateaus in all discharge curves from 0.1C to 3C, although the voltage polarization increased with the enlarged current rates. This result was still significantly better than that of S@CN-ns. As an example, at a current rate of 1C, the second plateau of S@CN-ns disappeared due to severe polarization, and the capacity could



not be released at 2C due to excessively high polarization (Figure S6). Therefore, it can be concluded that the S@CN-nt electrode effectively reduces the polarization voltage during the Li-S reaction, promoting the conversion process of LiPS.

Cycle stability is an important indicator for evaluating the performance of LSB. A 500-cycle stability test was conducted on the CN-nt host under a high current rate of 3C. In addition, S@CN-nt were still able to release a capacity of 636.8 mAh g<sup>-1</sup>, with a capacity retention of about 87.8% and an average Coulombic efficiency as high as 99.5%. Such excellent cycle stability can be attributed to the tubular hollow structure that cushions the volume expansion during Li-S conversion, as well as the high specific surface area and abundant pyrrolic-N active sites that anchor LiPS and suppress the shuttle effect. Table S2 in the Supporting Information displays a comparison of several parameters of state-of-the-art g-C<sub>3</sub>N<sub>4</sub>-based materials as cathode hosts for LSBs. It can be found that the CN-nt host presented here is characterized by competitive capacities and stabilities.

To meet the future commercial demands of LSBs, it is necessary to detect the performance under higher areal sulfur loading conditions. Therefore, cathodes with a sulfur loading of up to 3.5 mg cm<sup>-2</sup> were produced and electrochemically tested. As shown in Figure 4g, S@CN-nt exhibited an initial capacity of 805.9 mAh g<sup>-1</sup> at a current rate of 0.5 C and achieved a cycle stability of 74.8% after 100 cycles. The charge–discharge curves at 0.5 C with low/high-sulfur loading conditions were compared, as shown in Figure S7. Higher voltage polarization is caused under high-sulfur loading conditions. This is mainly due to the challenge of electron transfer and ion transport caused by thickened electrodes [48–50]. At the same time, more polysulfide compounds will be produced on the cathode during the charging and discharging process, while higher current density on the anode side will exacerbate the growth and pulverization of lithium dendrites. Therefore, such a good cyclic stability of the S@CN-nt electrode under high-sulfur loading conditions demonstrates that CN-nt act as a host material that could promote the release of the capacity of sulfur active materials, inhibit shuttle effects, and maintain stability during cycling. Thus, it is a suitable metal-free host material for LSBs.

#### 4. Conclusions

In conclusion, this study presents a one-step method for obtaining tubular CN-nt through precursor modification. In comparison to conventionally obtained CN-ns, CN-nt offer distinct advantages in terms of specific surface area and pore volume. This leads to improved distribution of sulfur, enhancing the utilization of active materials and suppressing volume expansion during the Li-S reaction. The interconnected porous structure also facilitates the diffusion of Li<sup>+</sup> ions. Additionally, the abundant pyridinic-N active sites play a crucial role in inhibiting the diffusion of LiPS, thereby ensuring a stable battery capacity. Leveraging these advantages, the S@CN-nt electrode exhibits robust performance, including high initial capacity and an ultra-low decay rate, surpassing that of the CN-ns host. This study highlights the effective regulation of g-C<sub>3</sub>N<sub>4</sub> nanostructures by controlling precursors, offering insights into the preparation of metal-free host materials for application in LSBs.

**Supplementary Materials:** The following supporting information can be downloaded at: <https://www.mdpi.com/article/10.3390/en16124545/s1>, Figure S1 SEM and EDS mapping images of CN-ns. Figure S2 XPS survey spectra of CN-ns and CN-nt. Figure S3 (a) XRD pattern of S@CN-nt. (b) TGA test under N<sub>2</sub> atmosphere of S@CN-nt. (c) SEM and EDS mapping images of S@CN-nt. Figure S4 (a) XRD pattern of S@CN-ns. (b) TGA test under N<sub>2</sub> atmosphere of S@CN-ns. (c) SEM and EDS mapping images of S@CN-ns. Figure S5 CV curves of CN-nt symmetrical cells without the presence of Li<sub>2</sub>S<sub>6</sub>. Figure S6 Charge/discharge curves of S@CN-ns at different current rates. Figure S7 Charge/discharge curves of S@CN-ns at 0.5 C with different sulfur loadings. Table S1. Comparison of precursor, specific surface area, and pore volume of CN-nt with previously reported g-C<sub>3</sub>N<sub>4</sub> materials obtained by different calcination methods. Table S2. Comparison of CN-nt electrochemical performance as host cathode for LSBs with state-of-the-art C<sub>3</sub>N<sub>4</sub>-based materials. References [51–67] are cited in the Supplementary Materials.

**Author Contributions:** Conceptualization, C.Z. (Chaoqi Zhang), J.J.B., and A.C.; methodology, C.Z. (Chaoqi Zhang), R.D., and K.X.; software, C.Z. (Chaoqi Zhang); validation, C.Z. (Chaoqi Zhang), C.Z. (Chaoyue Zhang), R.H., and C.L.; formal analysis, C.Z. (Chaoqi Zhang), and S.M.-S.; investigation, C.Z. (Chaoqi Zhang), R.D., S.M.-S., K.X., D.Y., C.Z. (Chaoyue Zhang), C.L., G.Z., X.C., R.H., J.A. and J.L.; resources, J.J.B. and A.C.; writing—original draft preparation, C.Z. (Chaoqi Zhang); writing—review and editing, A.C., J.A., and J.J.B.; visualization, C.Z. (Chaoqi Zhang) and S.M.-S.; supervision, A.C., J.A., and J.J.B.; project administration, A.C. and J.J.B.; funding acquisition, A.C. and J.J.B. All authors have read and agreed to the published version of the manuscript.

**Funding:** The authors thank the support from the project COMBENERGY, PID2019-105490RB-C32, from the Spanish Ministerio de Ciencia e Innovación. The authors acknowledge funding from Generalitat de Catalunya 2021 SGR 01581 and 2021 SGR 00457. ICN2 acknowledges the Severo Ochoa program from Spanish MINECO (Grant No. SEV-2017-0706). IREC and ICN2 are funded by the CERCA Programme from the Generalitat de Catalunya. ICN2 is supported by the Severo Ochoa program from Spanish MCIN/AEI (Grant No. CEX2021-001214-S). ICN2 acknowledges funding from Generalitat de Catalunya 2017 SGR 327. This study was supported by MCIN with funding from European Union NextGenerationEU (PRTR-C17.I1) and Generalitat de Catalunya. The authors thank the support from the project NANOGEN (PID2020-116093RB-C43), funded by MCIN/AEI/10.13039/501100011033/ and by “ERDF A way of making Europe”, by the “European Union”. This work was supported by the Natural Science Foundation of Sichuan province (NSFSC) and funded by the Science and Technology Department of Sichuan Province (2022NSFSC1229). The authors acknowledge scholarship from the China Scholarship Council (201706650011).

**Data Availability Statement:** Data are contained within the article or supplementary material.

**Conflicts of Interest:** The authors declare no conflict of interest.

## References

1. Blomgren, G.E. The Development and Future of Lithium Ion Batteries. *J. Electrochem. Soc.* **2016**, *164*, A5019. [[CrossRef](#)]
2. Xie, J.; Lu, Y.-C. A Retrospective on Lithium-Ion Batteries. *Nat. Commun.* **2020**, *11*, 2499. [[CrossRef](#)]
3. Seh, Z.W.; Sun, Y.; Zhang, Q.; Cui, Y. Designing High-Energy Lithium–Sulfur Batteries. *Chem. Soc. Rev.* **2016**, *45*, 5605–5634. [[CrossRef](#)] [[PubMed](#)]
4. Li, M.; Lu, J.; Chen, Z.; Amine, K. 30 Years of Lithium-Ion Batteries. *Adv. Mater.* **2018**, *30*, 1800561. [[CrossRef](#)]
5. Manthiram, A.; Chung, S.-H.; Zu, C. Lithium–Sulfur Batteries: Progress and Prospects. *Adv. Mater.* **2015**, *27*, 1980–2006. [[CrossRef](#)]
6. Eftekhari, A.; Kim, D.-W. Cathode Materials for Lithium–Sulfur Batteries: A Practical Perspective. *J. Mater. Chem. A* **2017**, *5*, 17734–17776. [[CrossRef](#)]
7. Yang, D.; Li, M.; Zheng, X.; Han, X.; Zhang, C.; Jacas Biendicho, J.; Llorca, J.; Wang, J.; Hao, H.; Li, J.; et al. Phase Engineering of Defective Copper Selenide toward Robust Lithium–Sulfur Batteries. *ACS Nano* **2022**, *16*, 11102–11114. [[CrossRef](#)]
8. Fei, B.; Zhang, C.; Cai, D.; Zheng, J.; Chen, Q.; Xie, Y.; Zhu, L.; Cabot, A.; Zhan, H. Hierarchical Nanoreactor with Multiple Adsorption and Catalytic Sites for Robust Lithium–Sulfur Batteries. *ACS Nano* **2021**, *15*, 6849–6860. [[CrossRef](#)] [[PubMed](#)]
9. Li, M.; Yang, D.; Biendicho, J.J.; Han, X.; Zhang, C.; Liu, K.; Diao, J.; Li, J.; Wang, J.; Heggen, M.; et al. Enhanced Polysulfide Conversion with Highly Conductive and Electrocatalytic Iodine-Doped Bismuth Selenide Nanosheets in Lithium–Sulfur Batteries. *Adv. Funct. Mater.* **2022**, *32*, 2200529. [[CrossRef](#)]
10. Zhang, C.Y.; Zhang, C.; Pan, J.L.; Sun, G.W.; Shi, Z.; Li, C.; Chang, X.; Sun, G.Z.; Zhou, J.Y.; Cabot, A. Surface Strain-Enhanced MoS<sub>2</sub> as a High-Performance Cathode Catalyst for Lithium–Sulfur Batteries. *eScience* **2022**, *2*, 405–415. [[CrossRef](#)]
11. Xu, H.; Kong, Z.; Siegenthaler, J.; Zheng, B.; Tong, Y.; Li, J.; Schuelke, T.; Fan, Q.H.; Wang, K.; Xu, H.; et al. Review on Recent Advances in Two-Dimensional Nanomaterials-Based Cathodes for Lithium-Sulfur Batteries. *EcoMat* **2023**, *5*, e12286. [[CrossRef](#)]
12. Xu, Z.-L.; Kim, J.-K.; Kang, K. Carbon Nanomaterials for Advanced Lithium Sulfur Batteries. *Nano Today* **2018**, *19*, 84–107. [[CrossRef](#)]
13. Wang, J.; Han, W.-Q. A Review of Heteroatom Doped Materials for Advanced Lithium–Sulfur Batteries. *Adv. Funct. Mater.* **2022**, *32*, 2107166. [[CrossRef](#)]
14. Wang, Y.; Liu, L.; Ma, T.; Zhang, Y.; Huang, H. 2D Graphitic Carbon Nitride for Energy Conversion and Storage. *Adv. Funct. Mater.* **2021**, *31*, 2102540. [[CrossRef](#)]
15. Zuo, Y.; Xu, X.; Zhang, C.; Li, J.; Du, R.; Wang, X.; Han, X.; Arbiol, J.; Llorca, J.; Liu, J.; et al. SnS<sub>2</sub>/g-C<sub>3</sub>N<sub>4</sub>/Graphite Nanocomposites as Durable Lithium-Ion Battery Anode with High Pseudocapacitance Contribution. *Electrochim. Acta* **2020**, *349*, 136369. [[CrossRef](#)]
16. Sun, W.; Song, Z.; Feng, Z.; Huang, Y.; Xu, Z.J.; Lu, Y.-C.; Zou, Q. Carbon-Nitride-Based Materials for Advanced Lithium–Sulfur Batteries. *Nano-Micro Lett.* **2022**, *14*, 222. [[CrossRef](#)] [[PubMed](#)]

17. Liang, Z.; Yang, D.; Tang, P.; Zhang, C.; Biendicho, J.J.; Zhang, Y.; Llorca, J.; Wang, X.; Li, J.; Heggen, M.; et al. Atomically Dispersed Fe in a C<sub>2</sub>N Based Catalyst as a Sulfur Host for Efficient Lithium–Sulfur Batteries. *Adv. Energy Mater.* **2020**, *11*, 2003507. [[CrossRef](#)]
18. Zhang, P.; Wang, F.; Qin, Y.; Wang, N. Exfoliated Graphitic Carbon Nitride Nanosheets/Gold Nanoparticles/Spherical Montmorillonite Ternary Porous Heterostructures for the Degradation of Organic Dyes. *ACS Appl. Nano Mater.* **2020**, *3*, 7847–7857. [[CrossRef](#)]
19. Du, R.; Xiao, K.; Li, B.; Han, X.; Zhang, C.; Wang, X.; Zuo, Y.; Guardia, P.; Li, J.; Chen, J.; et al. Controlled Oxygen Doping in Highly Dispersed Ni-Loaded g-C<sub>3</sub>N<sub>4</sub> Nanotubes for Efficient Photocatalytic H<sub>2</sub>O<sub>2</sub> Production. *Chem. Eng. J.* **2022**, *441*, 135999. [[CrossRef](#)]
20. Jun, Y.-S.; Park, J.; Lee, S.U.; Thomas, A.; Hong, W.H.; Stucky, G.D. Three-Dimensional Macroscopic Assemblies of Low-Dimensional Carbon Nitrides for Enhanced Hydrogen Evolution. *Angew. Chem.* **2013**, *125*, 11289–11293. [[CrossRef](#)]
21. Chen, F.; Liu, L.-L.; Wu, J.-H.; Rui, X.-H.; Chen, J.-J.; Yu, Y. Single-Atom Iron Anchored Tubular g-C<sub>3</sub>N<sub>4</sub> Catalysts for Ultrafast Fenton-Like Reaction: Roles of High-Valency Iron-Oxo Species and Organic Radicals. *Adv. Mater.* **2022**, *34*, 2202891. [[CrossRef](#)] [[PubMed](#)]
22. Wang, Z.; Huang, Y.; Chen, M.; Shi, X.; Zhang, Y.; Cao, J.; Ho, W.; Lee, S.C. Roles of N-Vacancies over Porous g-C<sub>3</sub>N<sub>4</sub> Microtubes during Photocatalytic NO<sub>x</sub> Removal. *ACS Appl. Mater. Interfaces* **2019**, *11*, 10651–10662. [[CrossRef](#)]
23. Iqbal, O.; Ali, H.; Li, N.; Ansari, M.Z.; Al-Sulami, A.I.; Alshammari, K.F.; Abd-Rabboh, H.S.M.; Al-Hadeethi, Y.; Taha, T.A.; Zada, A.; et al. A Review on the Synthesis, Properties, and Characterizations of Graphitic Carbon Nitride (g-C<sub>3</sub>N<sub>4</sub>) for Energy Conversion and Storage Applications. *Mater. Today Phys.* **2023**, *34*, 101080. [[CrossRef](#)]
24. Han, Z.; Wang, N.; Fan, H.; Ai, S. Ag Nanoparticles Loaded on Porous Graphitic Carbon Nitride with Enhanced Photocatalytic Activity for Degradation of Phenol. *Solid State Sci.* **2017**, *65*, 110–115. [[CrossRef](#)]
25. Xue, J.; Ma, S.; Zhou, Y.; Zhang, Z.; He, M. Facile Photochemical Synthesis of Au/Pt/g-C<sub>3</sub>N<sub>4</sub> with Plasmon-Enhanced Photocatalytic Activity for Antibiotic Degradation. *ACS Appl. Mater. Interfaces* **2015**, *7*, 9630–9637. [[CrossRef](#)]
26. Liu, Y.; Han, J.; Zeng, X.; Tian, Z.; Yu, F.; Sun, X.; Liu, Q.; Wang, W. G-C<sub>3</sub>N<sub>4</sub> Homophase Junction with High Crystallinity Using MoS<sub>2</sub> as Cocatalyst for Robust Visible-Light-Driven Photocatalytic Pollutant Degradation. *ChemistrySelect* **2022**, *7*, e202103884. [[CrossRef](#)]
27. Zhang, C.; Du, R.; Biendicho, J.J.; Yi, M.; Xiao, K.; Yang, D.; Zhang, T.; Wang, X.; Arbiol, J.; Llorca, J.; et al. Tubular CoFeP@CN as a Mott–Schottky Catalyst with Multiple Adsorption Sites for Robust Lithium–Sulfur Batteries. *Adv. Energy Mater.* **2021**, *11*, 2100432. [[CrossRef](#)]
28. Zhang, D.; Wang, S.; Hu, R.; Gu, J.; Cui, Y.; Li, B.; Chen, W.; Liu, C.; Shang, J.; Yang, S. Catalytic Conversion of Polysulfides on Single Atom Zinc Implanted MXene toward High-Rate Lithium–Sulfur Batteries. *Adv. Funct. Mater.* **2020**, *30*, 2002471. [[CrossRef](#)]
29. Zhang, C.; Biendicho, J.J.; Zhang, T.; Du, R.; Li, J.; Yang, X.; Arbiol, J.; Zhou, Y.; Morante, J.R.; Cabot, A. Combined High Catalytic Activity and Efficient Polar Tubular Nanostructure in Urchin-Like Metallic NiCo<sub>2</sub>Se<sub>4</sub> for High-Performance Lithium–Sulfur Batteries. *Adv. Funct. Mater.* **2019**, *29*, 1903842. [[CrossRef](#)]
30. Liu, D.; Zhang, C.; Zhou, G.; Lv, W.; Ling, G.; Zhi, L.; Yang, Q.-H. Catalytic Effects in Lithium–Sulfur Batteries: Promoted Sulfur Transformation and Reduced Shuttle Effect. *Adv. Sci.* **2018**, *5*, 1700270. [[CrossRef](#)]
31. Wang, P.; Xi, B.; Huang, M.; Chen, W.; Feng, J.; Xiong, S. Emerging Catalysts to Promote Kinetics of Lithium–Sulfur Batteries. *Adv. Energy Mater.* **2021**, *11*, 2002893. [[CrossRef](#)]
32. Yang, D.; Liang, Z.; Zhang, C.; Biendicho, J.J.; Botifoll, M.; Spadaro, M.C.; Chen, Q.; Li, M.; Ramon, A.; Moghaddam, A.O.; et al. NbSe<sub>2</sub> Meets C<sub>2</sub>N: A 2D-2D Heterostructure Catalysts as Multifunctional Polysulfide Mediator in Ultra-Long-Life Lithium–Sulfur Batteries. *Adv. Energy Mater.* **2021**, *11*, 2101250. [[CrossRef](#)]
33. Zhang, T.; Shao, W.; Liu, S.; Song, Z.; Mao, R.; Jin, X.; Jian, X.; Hu, F. A Flexible Design Strategy to Modify Ti<sub>3</sub>C<sub>2</sub>T<sub>x</sub> MXene Surface Terminations via Nucleophilic Substitution for Long-Life Li-S Batteries. *J. Energy Chem.* **2022**, *74*, 349–358. [[CrossRef](#)]
34. Chen, Z.-X.; Zhang, Y.-T.; Bi, C.-X.; Zhao, M.; Zhang, R.; Li, B.-Q.; Huang, J.-Q. Premature Deposition of Lithium Polysulfide in Lithium–Sulfur Batteries. *J. Energy Chem.* **2023**, *82*, 507–512. [[CrossRef](#)]
35. Fan, F.Y.; Carter, W.C.; Chiang, Y.-M. Mechanism and Kinetics of Li<sub>2</sub>S Precipitation in Lithium-Sulfur Batteries. *Adv. Mater.* **2015**, *27*, 5203–5209. [[CrossRef](#)]
36. Yuan, H.; Peng, H.-J.; Li, B.-Q.; Xie, J.; Kong, L.; Zhao, M.; Chen, X.; Huang, J.-Q.; Zhang, Q. Conductive and Catalytic Triple-Phase Interfaces Enabling Uniform Nucleation in High-Rate Lithium-Sulfur Batteries. *Adv. Energy Mater.* **2018**, *9*, 1802768. [[CrossRef](#)]
37. Zhang, C.; Chen, Q.; Zhan, H. Supercapacitors Based on Reduced Graphene Oxide Nanofibers Supported Ni(OH)<sub>2</sub> Nanoplates with Enhanced Electrochemical Performance. *ACS Appl. Mater. Interfaces* **2016**, *8*, 22977–22987. [[CrossRef](#)]
38. Li, J.; Li, L.; Ma, X.; Han, X.; Xing, C.; Qi, X.; He, R.; Arbiol, J.; Pan, H.; Zhao, J.; et al. Selective Ethylene Glycol Oxidation to Formate on Nickel Selenide with Simultaneous Evolution of Hydrogen. *Adv. Sci.* **2023**, *10*, 2300841. [[CrossRef](#)]
39. Zhao, M.; Tan, P.; Cai, D.; Liu, Y.; Zhang, C.; Fei, B.; Sa, B.; Chen, Q.; Zhan, H. Customizing Component Regulated Dense Heterointerfaces for Crafting Robust Lithium-Sulfur Batteries. *Adv. Funct. Mater.* **2023**, *33*, 2211505. [[CrossRef](#)]
40. Fu, J.; Shen, Z.; Cai, D.; Fei, B.; Zhang, C.; Wang, Y.; Chen, Q.; Zhan, H. A Hierarchical VN/Co<sub>3</sub>ZnCN@NCNT Composite as a Multifunctional Integrated Host for Lithium–Sulfur Batteries with Enriched Adsorption Sites and Accelerated Conversion Kinetics. *J. Mater. Chem. A* **2022**, *10*, 20525–20534. [[CrossRef](#)]

41. Zhang, C.Y.; Zhang, C.; Sun, G.W.; Pan, J.L.; Gong, L.; Sun, G.Z.; Biendicho, J.J.; Balcells, L.; Fan, X.L.; Morante, J.R.; et al. Spin Effect to Promote Reaction Kinetics and Overall Performance of Lithium-Sulfur Batteries under External Magnetic Field. *Angew. Chem. Int. Ed.* **2022**, *61*, e202211570. [[CrossRef](#)] [[PubMed](#)]
42. Yu, X.; Zhang, C.; Luo, Z.; Zhang, T.; Liu, J.; Li, J.; Zuo, Y.; Biendicho, J.J.; Llorca, J.; Arbiol, J.; et al. A Low Temperature Solid State Reaction to Produce Hollow  $\text{MnxFe}_3\text{-XO}_4$  Nanoparticles as Anode for Lithium-Ion Batteries. *Nano Energy* **2019**, *66*, 104199. [[CrossRef](#)]
43. Zhang, C.; Fei, B.; Yang, D.; Zhan, H.; Wang, J.; Diao, J.; Li, J.; Henkelman, G.; Cai, D.; Biendicho, J.J.; et al. Robust Lithium-Sulfur Batteries Enabled by Highly Conductive  $\text{WSe}_2$ -Based Superlattices with Tunable Interlayer Space. *Adv. Funct. Mater.* **2022**, *32*, 2201322. [[CrossRef](#)]
44. Qie, L.; Zu, C.; Manthiram, A. A High Energy Lithium-Sulfur Battery with Ultrahigh-Loading Lithium Polysulfide Cathode and Its Failure Mechanism. *Adv. Energy Mater.* **2016**, *6*, 1502459. [[CrossRef](#)]
45. Yang, J.; Xu, L.; Li, S.; Peng, C. The Role of Titanium-Deficient Anatase  $\text{TiO}_2$  Interlayers in Boosting Lithium-Sulfur Battery Performance: Polysulfide Trapping, Catalysis and Enhanced Lithium Ion Transport. *Nanoscale* **2020**, *12*, 4645–4654. [[CrossRef](#)]
46. Yang, D.; Liang, Z.; Tang, P.; Zhang, C.; Tang, M.; Li, Q.; Biendicho, J.J.; Li, J.; Heggen, M.; Dunin-Borkowski, R.E.; et al. A High Conductivity 1D  $\pi$ -d Conjugated Metal-Organic Framework with Efficient Polysulfide Trapping-Diffusion-Catalysis in Lithium-Sulfur Batteries. *Adv. Mater.* **2022**, *34*, 2108835. [[CrossRef](#)]
47. Chu, R.; Nguyen, T.T.; Bai, Y.; Kim, N.H.; Lee, J.H. Uniformly Controlled Treble Boundary Using Enriched Adsorption Sites and Accelerated Catalyst Cathode for Robust Lithium-Sulfur Batteries. *Adv. Energy Mater.* **2022**, *12*, 2102805. [[CrossRef](#)]
48. Lv, D.; Zheng, J.; Li, Q.; Xie, X.; Ferrara, S.; Nie, Z.; Mehdi, L.B.; Browning, N.D.; Zhang, J.-G.; Graff, G.L.; et al. High Energy Density Lithium-Sulfur Batteries: Challenges of Thick Sulfur Cathodes. *Adv. Energy Mater.* **2015**, *5*, 1402290. [[CrossRef](#)]
49. Wu, J.; Zhang, X.; Ju, Z.; Wang, L.; Hui, Z.; Mayilvahanan, K.; Takeuchi, K.J.; Marschilok, A.C.; West, A.C.; Takeuchi, E.S.; et al. From Fundamental Understanding to Engineering Design of High-Performance Thick Electrodes for Scalable Energy-Storage Systems. *Adv. Mater.* **2021**, *33*, 2101275. [[CrossRef](#)]
50. Zheng, H.; Li, J.; Song, X.; Liu, G.; Battaglia, V.S. A Comprehensive Understanding of Electrode Thickness Effects on the Electrochemical Performances of Li-Ion Battery Cathodes. *Electrochim. Acta* **2012**, *71*, 258–265. [[CrossRef](#)]
51. Dong, F.; Sun, Y.; Wu, L.; Fu, M.; Wu, Z. Facile Transformation of Low Cost Thiourea into Nitrogen-Rich Graphitic Carbon Nitride Nanocatalyst with High Visible Light Photocatalytic Performance. *Catal. Sci. Technol.* **2012**, *2*, 1332–1335. [[CrossRef](#)]
52. Li, Y.; Sun, Y.; Ho, W.; Zhang, Y.; Huang, H.; Cai, Q.; Dong, F. Highly Enhanced Visible-Light Photocatalytic  $\text{NO}_x$  Purification and Conversion Pathway on Self-Structurally Modified  $\text{g-C}_3\text{N}_4$  Nanosheets. *Sci. Bull.* **2018**, *63*, 609–620. [[CrossRef](#)]
53. Cui, Y.; Zhang, G.; Lin, Z.; Wang, X. Condensed and Low-Defected Graphitic Carbon Nitride with Enhanced Photocatalytic Hydrogen Evolution under Visible Light Irradiation. *Appl. Catal. B Environ.* **2016**, *181*, 413–419. [[CrossRef](#)]
54. Zhang, Y.; Liu, J.; Wu, G.; Chen, W. Porous Graphitic Carbon Nitride Synthesized via Direct Polymerization of Urea for Efficient Sunlight-Driven Photocatalytic Hydrogen Production. *Nanoscale* **2012**, *4*, 5300–5303. [[CrossRef](#)] [[PubMed](#)]
55. Jia, Z.; Zhang, H.; Yu, Y.; Chen, Y.; Yan, J.; Li, X.; Zhang, H. Trithiocyanuric Acid Derived  $\text{g-C}_3\text{N}_4$  for Anchoring the Polysulfide in Li-S Batteries Application. *J. Energy Chem.* **2020**, *43*, 71–77. [[CrossRef](#)]
56. Li, X.; Hartley, G.; Ward, A.J.; Young, P.A.; Masters, A.F.; Maschmeyer, T. Hydrogenated Defects in Graphitic Carbon Nitride Nanosheets for Improved Photocatalytic Hydrogen Evolution. *J. Phys. Chem. C* **2015**, *119*, 14938–14946. [[CrossRef](#)]
57. Xu, H.; Yan, J.; She, X.; Xu, L.; Xia, J.; Xu, Y.; Song, Y.; Huang, L.; Li, H. Graphene-Analogue Carbon Nitride: Novel Exfoliation Synthesis and Its Application in Photocatalysis and Photoelectrochemical Selective Detection of Trace Amount of  $\text{Cu}^{2+}$ . *Nanoscale* **2014**, *6*, 1406–1415. [[CrossRef](#)]
58. Ma, H.; Li, Y.; Li, S.; Liu, N. Novel PO Codoped  $\text{G-C}_3\text{N}_4$  with Large Specific Surface Area: Hydrothermal Synthesis Assisted by Dissolution-Precipitation Process and Their Visible Light Activity under Anoxic Conditions. *Appl. Surf. Sci.* **2015**, *357*, 131–138. [[CrossRef](#)]
59. Wang, Y.; Wang, X.; Antonietti, M.; Zhang, Y. Facile One-Pot Synthesis of Nanoporous Carbon Nitride Solids by Using Soft Templates. *ChemSusChem* **2010**, *3*, 435–439. [[CrossRef](#)]
60. Li, X.-H.; Wang, X.; Antonietti, M. Mesoporous  $\text{G-C}_3\text{N}_4$  Nanorods as Multifunctional Supports of Ultrafine Metal Nanoparticles: Hydrogen Generation from Water and Reduction of Nitrophenol with Tandem Catalysis in One Step. *Chem. Sci.* **2012**, *3*, 2170–2174. [[CrossRef](#)]
61. Lee, E.Z.; Jun, Y.-S.; Hong, W.H.; Thomas, A.; Jin, M.M. Cubic Mesoporous Graphitic Carbon(IV) Nitride: An All-in-One Chemosensor for Selective Optical Sensing of Metal Ions. *Angew. Chem.* **2010**, *122*, 9900–9904. [[CrossRef](#)]
62. Wang, J.; Meng, Z.; Yang, W.; Yan, X.; Guo, R.; Han, W.-Q. Facile Synthesis of RGO/ $\text{g-C}_3\text{N}_4$ /CNT Microspheres via an Ethanol-Assisted Spray-Drying Method for High-Performance Lithium-Sulfur Batteries. *ACS Appl. Mater. Interfaces* **2019**, *11*, 819–827. [[CrossRef](#)] [[PubMed](#)]
63. Pang, Q.; Nazar, L.F. Long-Life and High-Areal-Capacity Li-S Batteries Enabled by a Light-Weight Polar Host with Intrinsic Polysulfide Adsorption. *ACS Nano* **2016**, *10*, 4111–4118. [[CrossRef](#)] [[PubMed](#)]
64. Zhang, H.; Zhao, Z.; Hou, Y.-N.; Tang, Y.; Dong, Y.; Wang, S.; Hu, X.; Zhang, Z.; Wang, X.; Qiu, J. Nanopore-Confined  $\text{g-C}_3\text{N}_4$  Nanodots in N, S Co-Doped Hollow Porous Carbon with Boosted Capacity for Lithium-Sulfur Batteries. *J. Mater. Chem. A* **2018**, *6*, 7133–7141. [[CrossRef](#)]



65. Zhang, H.; Lin, X.; Li, J.; Han, T.; Zhu, M.; Xu, X.; Hu, C.; Liu, J. A Binder-Free Lithium-Sulfur Battery Cathode Using Three-Dimensional Porous g-C<sub>3</sub>N<sub>4</sub> Nanoflakes as Sulfur Host Displaying High Binding Energies with Lithium Polysulfides. *J. Alloys Compd.* **2021**, *881*, 160629. [[CrossRef](#)]
66. Wang, W.; Dong, W.; Hong, X.; Liu, Y.; Yang, S. Preparation of G-C<sub>3</sub>N<sub>4</sub>/CNTs Composite by Dissolution-Precipitation Method as Sulfur Host for High-Performance Lithium-Sulfur Batteries. *Mater. Chem. Phys.* **2022**, *283*, 126014. [[CrossRef](#)]
67. Moon, S.-H.; Shin, J.-H.; Kim, J.-H.; Jang, J.-S.; Kim, S.-B.; Park, Y.-Y.; Lee, S.-N.; Park, K.-W. Polypyrrole Coated G-C<sub>3</sub>N<sub>4</sub>/RGO/S Composite as Sulfur Host for High Stability Lithium-Sulfur Batteries. *Mater. Chem. Phys.* **2022**, *287*, 126267. [[CrossRef](#)]

**Disclaimer/Publisher's Note:** The statements, opinions and data contained in all publications are solely those of the individual author(s) and contributor(s) and not of MDPI and/or the editor(s). MDPI and/or the editor(s) disclaim responsibility for any injury to people or property resulting from any ideas, methods, instructions or products referred to in the content.